Pattern Recognition Letters 45 (2014) 181–188

Contents lists available at ScienceDirect

Pattern Recognition Letters

journal homepage: www.elsevier.com/locate/patrec

Digital flow for shape decomposition: Application to 3-D microtomographic images of snow ☆

Xi Wang [a,b,c,*], David Coeurjolly [a], Frédéric Flin [b]

[a] CNRS – LIRIS, UMR 5205, F-69622, France
[b] Météo-France – CNRS, CNRM – GAME, UMR 3589, CEN, F-38400, France[1]
[c] Université Paul Sabatier, Toulouse F-31062, France

ARTICLE INFO

Article history:
Received 27 August 2013
Available online 24 March 2014

Keywords:
Medial axis
Digital flow
Shape decomposition
Snow microstructure

ABSTRACT

We propose a fast shape decomposition method for granular microstructures using a 3-D approach based on medial axis. We define a two-step algorithm: the first step relies on a notion of digital flow to obtain a preliminary over-decomposition from medial balls. During a second step, we use geometric criteria to obtain a relevant and precise volumetric decomposition. We apply our algorithm to 3-D objects of materials and, more precisely, to microtomographic images of snow microstructures.

1. Introduction

Shape decomposition is one of the fundamental techniques in computer graphics and is widely used in shape processing. The goal of decomposition, sometimes called *segmentation*, is to simplify and/or change the representation of an object in order to make it more meaningful and easy to analyze [33]. The principal contribution of this paper focuses on a fast and efficient shape decomposition method which is based on the digital flow. The concept of flow was introduced in [12]. With the proposition of a fast computation of critical points in digital domain, we obtain a framework of method which is optimal in time. Moreover, we provide two distinct geometrical criteria to control the quality of the decomposition.

In this paper, we first propose a digital version of the flow notion from computational geometry to yield a fast initial decomposition of 3-D granular materials into regions (Section 4). This approach provides a structure on the initial regions which allows us to define a simple filtering algorithm to correct over-decomposition effects (Section 5). We validate the quality of the decomposition on both synthetic data and images of granular snow samples (Section 6).

2. Related works

The main context of this paper is the analysis of granular materials from 3-D computed tomographic images. More precisely, we focus on a specific granular material, i.e. *deposited snow on the ground* (see Fig. 9), which is observed at the scale of its *microstructure* (1 voxel $\sim$ 5–20 μm). In this context, micro-scale modelling requires a precise 3-D description of snow microstructures in terms of individual grains and bond's characteristics [6]. Practically, there are various shape types of snow present in the snowpack, like *Precipitation Particles* (PP), *Rounded Grains* (RG), *Melt Forms* (MF) and so on [15]. Each class implies different geometry of grains from nearly spherical objects to facetted ones. So the challenge is to decompose the 3-D images of these different snow types into grains, which are usually sintered together and form complex shapes. Another specific aspect of our context is that physical analysis of snow microstructures leads to further requirements on the grain-to-grain interfaces: the interface between two grains should be flat or with minimal curvature values. We do not use such an information directly in our segmentation approach but we rely on it in our experimental evaluation.

From image processing, several approaches for shape decomposition problems consider mathematical morphology tools such as watershed transform [13] or region growing operators [32]. In our context where the input object is a binary volume, the main idea of these approaches is to start from a set of markers defined by local maxima in the distance transform of the input shape (see [34,22] for a survey). Then, a propagation process is used to enlarge catchment basins of each local minimum to define the

☆ This paper has been recommended for acceptance by M. Couprie.
[1] CNRM-GAME/CEN is part of Labex OSUG@2020 (ANR10 LABX56).
* Corresponding author at: CNRS – LIRIS, UMR 5205, F-69622, France.
E-mail addresses: xi.wang@meteo.fr, xiwang.it@gmail.com (X. Wang), david.coeurjolly@liris.cnrs.fr (D. Coeurjolly), frederic.flin@meteo.fr (F. Flin).

http://dx.doi.org/10.1016/j.patrec.2014.03.005
0167-8655/

overall decomposition into non-overlapping regions. Despite several improvements [14], the main drawback is that such approaches have difficulties to capture the complex shape geometry of snow grains and bonds.

Surface based techniques can also be considered. The main idea is to perform a first decomposition on the 3-D object boundary and to propagate such decomposition to the object's interior to finally obtain the volumetric decomposition. If we suppose that grains are smooth with rounded shapes, differential estimators (mean and Gaussian curvatures) can be used to decompose the surface into components with almost constant curvature values [37]. In a previous work [36], we have developed such decomposition tools based on surface curvature information. This method identifies groove regions on the surface of object to locate the possible separating boundaries in volume. However, all these techniques are highly sensitive to the initial surface decomposition into groove regions from curvature map. Furthermore, they require stable and robust to noise differential curvature estimators, which could be challenging.

Another approach consists in decomposing the initial shape using volumetric information based on the distance map [35] or the medial axis representation of a shape [12]. For the first mentioned approach, the idea is close to the watershed approach: we start from local maxima of the distance map and we perform a propagation process to construct the regions. A last step is required to overcome the over-decomposition induced by the first step and uses a heuristic based merging process between adjacent regions. Similarly to watershed, the method is highly sensitive to the initial local maxima computation and the region interface quality is poor. From computational geometry, Dey et al. [12] proposed an interesting mathematical tool which constructs a continuous flow from the medial axis representation of a shape. In this approach, the object is represented by point sets on its boundary and the medial axis is defined as a subset of the Voronoi diagram of the input point set [3]. Another method which is based on curve skeletons was proposed by Reniers and Telea [27,28]. The curve-skeleton junctions which signal the interpenetration of parts are detected based on the junction rule using a function based geodesic metric to quantify the relevance of a given curve-skeleton branch. These approaches provide very good results on 3-D models and CAD shapes. However, when applying them to large microtomographic images of snow microstructures (high resolution objects, high topology genus, noisy curve-skeleton with small shortest loops associated to surface), these approaches become time consuming and may lead to inconsistent decomposition.

We propose here a purely volumetric approach which does not require to back-project volumetric information (curve-skeleton or medial structures) to the object surface to compute geometrical information. Our proposal is thus based on simple digital volumetric data structures (digital power map and digital flow), which can be obtained by very fast algorithms.

3. Preliminaries

In this section, we outline the notion of *Flow* induced by a shape [12]. The original *Flow* definition is described here in a more general setting by considering general shapes which are embedded in d-dimensional Euclidean space $\mathbb{R}^d$.

3.1. Flow in continuous space

In the following, $\mathcal{X}$ denotes a compact subset of d-dimensional Euclidean space $\mathbb{R}^d$, $\partial\mathcal{X}$ denotes its boundary. The definitions can be found in [12]. Given $\mathcal{X} \subset \mathbb{R}^d$, the *distance transform* $h : \mathbb{R}^d \to \mathbb{R}$ is defined at each point $x \in \mathbb{R}^d$ such that

$$h(x) = inf_{y\in\partial\mathcal{X}}\|y - x\|^2 \tag{1}$$

Definition 1 (*Anchor set*). For all $x \in \mathbb{R}^d$, the anchor set $A(x)$ of x is given by

$$A(x) = argmin_{y\in\partial\mathcal{X}}\|y - x\|^2 \tag{2}$$

In other words, $A(x)$ is the set of the closest points to x in $\partial\mathcal{X}$. Let $conv(A(x))$ be the convex hull of $A(x)$. In Fig. 1, we illustrate, in dimension 2, several configurations where $conv(A(x))$ is a triangle or an edge.

Definition 2 (*Critical and Regular points*). A point $x \in \mathbb{R}^d$ is a *critical point* if $x \in conv(A(x))$. Otherwise, x is regular.

The flow is defined by using the direction of steepest ascent. First, we set $d(x)$ as driver of x, where $d(x) = argmin_{y\in conv(A(x))}\|y - x\|^2 \ \forall\ x \in \mathbb{R}^d$. We then define a vector $v : \mathbb{R}^d \to \mathbb{R}^d$, $v(x) = \frac{x-d(x)}{\|x-d(x)\|}$ if $x \neq d(x)$ and 0 otherwise.

Definition 3 (*Induced Flow*). The flow is a function $\phi : [0,\infty) \times \mathbb{R}^d \to \mathbb{R}^d$, the right derivative of which satisfies, at each point $x \in \mathbb{R}^d$

$$\lim_{t\downarrow t_0}\frac{\phi(t,x) - \phi(t_0,x)}{t - t_0} = v(\phi(t_0,x)) \tag{3}$$

Definition 4 (*Stable manifold*). The stable manifold $S(x)$ of a critical point x is the set of all the points which flow into x.

$$S(x) = \{y \in \mathbb{R}^d : \lim_{t\to\infty}\phi(t,y) = x\} \tag{4}$$

The stable manifolds of all critical points induce a decomposition of the object into disjoint regions (the word *stable* thus refers to locii where the flow gradient is null). It means, $\mathbb{R}^d = \bigcup_x S(x)$ for all critical points x. Furthermore, the decomposition is valid since for any two critical points x and y ($x \neq y$), we have $S(x) \cap S(y) = \emptyset$.

3.2. Medial axis and digital medial axis

The Medial axis of a shape is a classic method for shape analysis. It was first proposed by Blum [4] in the continuous plane and can be defined as the set of balls contained in $\mathcal{X}$ touching at least twice $\partial\mathcal{X}$. Following previous definitions, a ball with center $x \in \mathcal{X}$ and radius r belongs to the medial axis if and only if $|A(x)| \geqslant 2$ and $\|y - x\| = r$ for any point $y \in A(x)$.

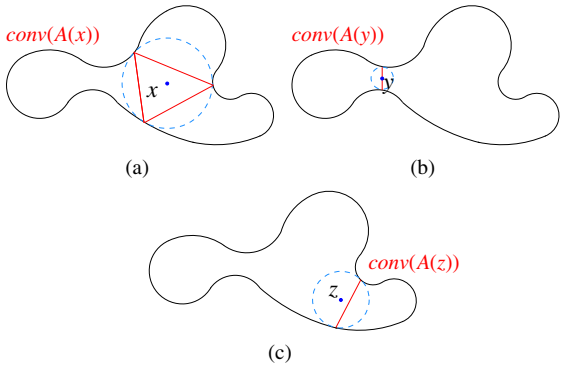

Fig. 1. Several configurations to illustrate the definition of critical points: In (a), x is such that $x \in conv(A(x))$ (triangle in red) and is thus a critical point. In (b), y lies in the segment $conv(A(y))$, y is a critical point too. In (c), $z \notin conv(A(z))$, so z is a regular point. (For interpretation of the references to color in this figure legend, the reader is referred to the web version of this article.)

When dealing with digital objects ($X \subset \mathbb{Z}^d$), an alternative definition has been proposed in the digital framework [23] using a notion of maximal ball:

Definition 5 (*Digital Medial Axis*). The *Digital Medial Axis* (MA for short) is defined as the set of maximal balls of X: a ball $B \subset X$ is maximal in X if there is no ball $B' \subset X$ such that $B \subset B'$.

$B(c,r)$ denotes an Euclidean open ball with center $c \in X$ and radius r.

From these definitions, many algorithms have been proposed to extract such medial axis structure [30,5,25,24,31,26,20,10]. In the following, we focus on the method of [10], which extracts the discrete medial axis of a shape $X \subset [1\dots n]^3$ in $O(n^3)$ optimal time.

4. Digital flow and flow based decomposition

Dey et al. [12] use the stable manifolds to decompose a shape represented by a point cloud sampling its surface. First, the authors construct the Delaunay triangulation of input points [3]. Delaunay triangulation is the dual structure of the Voronoi diagram. Both structures are cellular structures in the sense that they are defined as union of open i–facets with dimensions 0 to d. For instance, Delaunay triangulation in dimension 2 is made of triangles (2–facets), edges (1–facets) and vertices (0–facets). Voronoi diagram and its dual are meaningful in the flow context since the authors proved that:

Lemma 1 [12]. *Given a set of points $\mathcal{P}$ in $\mathbb{R}^d$ sampling the boundary of a shape $\mathcal{X}$, critical points for the flow induced by $\mathcal{P}$ are the Voronoi i–facets inside $\mathcal{X}$ intersecting their dual Delaunay $(d-i)$-facet.*

In other words, to decide if a Voronoi vertex x is a critical point, we have to check if x is inside the Delaunay triangle which is the dual of x (see Fig. 2). Using such result, Dey et al. approximate stable manifolds as connected sets of Delaunay i–facets. Furthermore, they proposed an algorithm to decompose an object defined by points on its boundary into regions, each region being a stable manifold or a union of stable manifolds. Indeed, they define a simple process to decide if two adjacent stable manifolds can be merged: along the interface between the two stable manifolds, the maximal distance function value h_{max} is computed. Then, the two regions are merged if the ratio between h_{max} and the distance function of each manifold critical point is below a given threshold. We will discuss about this heuristic in Section 5.2.

When considering a digital object X in dimension 3 and if we suppose that p is defined on a $[1\dots n]^3$ domain, we could directly use Lemma 1 and thus continuous Voronoi diagram and Delaunay triangulation to extract critical points and thus stable manifolds.

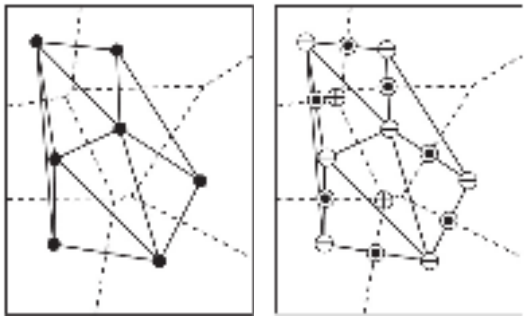

(a) (b)

Fig. 2. Voronoi diagram (dashed lines) and Delaunay triangulation (solid lines) of the points in $\mathbb{R}^2$ (a). The critical points (maxima ⊕, saddle point ⊙, minima ⊖) of the distance function induced by these seven points (b). (presented in [12]).

However, the overall computational time would be high since the Delaunay triangulation in 3D has a quadratic number, $O(N^2)$, of tetrahedrons if N is the number of the input points. In our case, N can be in $O(n^3)$ since the specific surface area (ratio between the shape surface area and the volume) can be high. For instance, the shape in Fig. 9(b) defined in volume with size 256^3 has 1144238 surface elements. Computing the complete Delaunay triangulation would be intractable for larger images.

We propose here a fast computation of critical points using tools working on the digital domain. More precisely, we describe an optimal in time $O(n^3)$ algorithm to extract digital critical points and digital stable manifolds. First of all, let us define an additional structure from computational geometry, the Power Diagram. Let us consider a set of N balls S defined by centers $\{c_i\}_{i=1\dots N}$ and radii $\{r_i\}_{i=1\dots N}$. The power distance $\pi_i(x)$ of a point $x \in \mathbb{R}^d$ to the ball (c_i, r_i) is defined by

$$\pi_i(x) = \|x - c_i\|^2 - r_i^2. \tag{5}$$

Hence, $\pi_i(x) < 0$ (resp. $\pi_i(x) > 0$) if x belongs to (resp. is outside of) the ball (c_i, r_i). The power diagram is a decomposition of the space into cells $Pow(\{c_i\},\{r_i\}) = \{\sigma_i\}_{i=1\dots N}$ such that $\sigma_i = \{x \in \mathbb{R}^d : \pi_i(x) \leqslant \pi_j(x), \forall j \neq i\}$. In other words, the Power Diagram is a Voronoi Diagram in which the Euclidean metric has been changed to a weighted additive one.

In digital geometry, algorithms exist to compute Voronoi [11,19] and Power mappings [10]. Such mappings differ from their respective diagram in the sense that the output is not a combinatorial structure but the intersection between the diagram and the grid. For instance, in addition to the discrete medial axis extraction, an algorithm proposed by Coeurjolly and Montanvert [10] also computes the digital Power map $\Pi_X : X \to \{1,\dots,N\}$ such that $\Pi_X = Pow(\{c_i\},\{r_i\}) \cap \mathbb{Z}^3 \cap X$ from medial balls $(\{c_i\},\{r_i\})$ in $O(n^3)$ optimal time. Hence, for each point $p \in X$, $\Pi_X(p)$ is the label of the power cell σ_i such that $p \in \sigma_i$ (if p belongs to power cell boundary, *i.e.* p is equi-distant, for the power metric, to two balls, we only return one of the adjacent power cells).

The algorithm described by Coeurjolly and Montanvert [10] is perfectly suited for processing large digital objects since it is based on simple 1D raster scans in the volume (each voxel is visited a constant number of times), which can be performed independently. Hence, such a technique allows us to design efficient multi-thread implementations to handle very large objects (an implementation is available in the `DGtal` library [9]).

To define digital critical points we use the following lemma which connects Power Diagram and Delaunay triangulation in computational geometry.

Lemma 2 [1]. *Let $\mathcal{P}$ be a set of points in general position in $\mathbb{R}^3$. Let $\mathcal{B}$ be the set of balls defined on Voronoi vertices of $\mathcal{P}$. The power diagram of $\mathcal{B}$ is the Delaunay triangulation of $\mathcal{P}$.*

Hence, instead of checking if a given Voronoi vertex v belongs to its dual Delaunay triangle in Lemma 1, we check if v belongs to its power diagram cell. We can now give our definition of digital critical points.

Definition 6 (*Digital Critical Point*). Let $X \subset [1\dots n]^3$ be a digital object and let $MA(X)$ be its digital medial axis and Π_X the digital power map of balls in $MA(X)$. Let c_i be a medial ball center, c_i is a *digital critical point* if $\Pi_X(c_i) = i$.

In other words, c_i is critical if $c_i \in \sigma_i$ in the digital domain (see Fig. 3).

In this digital setting, stable manifolds become union of power diagram cells. Let us first define the assignment of regular points to critical ones in a recursive way: let c_j be regular and let c_i be the

medial ball center such that $\Pi_X(c_j) = i$, if c_i is critical, we set $l(c_i) = i$, we attach σ_j to σ_i using a label function $l(c_j) = i$. If c_i is not critical, we set $l(c_j) = l(c_i)$. Even if sequences of regular points may appear when attaching a regular point to a critical one, such recursive definition makes sense only if there is no cycle of regular points in the label assignment. We never observe such cycles in our objects but if detected, a simple heuristic can be used to break it: we compute the minimum power distance between each regular point in the cycle and all critical balls. Then, if the minimum distance is given by the regular point c_j and critical point c_i, we force the assignment $l(c_j) = \Pi_X(c_i)$, breaking the cycle.

Definition 7 (*Digital Stable Manifolds*). Let c_i be a critical point, the *digital stable manifold* of c_i, denoted $F(c_i)$ is given by

$$F(c_i) = \{p \in X \,|\, \Pi_X(p) = j \text{ and } l(c_j) = i\} \tag{6}$$

The construction of the digital stable manifold is depicted in Fig. 4.

5. Main algorithm

The overall algorithm can be described as follows: starting from a binary object X, we first compute its medial axis $MA(X)$ and power map Π_X using the method of [10] (see Fig. 5). Then we use Def. 6 to detect critical points in $MA(X)$. At this step, digital stable manifolds (Definition 7) give us a first decomposition of X which is consistent with the distance flow induced by X (see for example Fig. 7(a)). At this point, the overall decomposition is consistent in the sense that it is volumetric, the union of all regions covers the input shape and all regions are disjoint.

However, an over-decomposition, i.e. a decomposition which segments a shape unnecessarily into very small features is generally obtained at this stage. It is thus important to merge all mergeable stable manifolds together. This step is ensured by filtering the medial axis (condition on the balls' size – Section 5.1) and by using a simple geometrical criterion based on ball intersection geometry (Section 5.2).

5.1. Pre-processing

When dealing with noisy data, the small perturbations change the medial axis of a shape and then lead to many small balls on the boundary or near sharp features (see Fig. 5(b)) which are not desirable. In many cases, MA based algorithms have to filter the output to only keep relevant MA balls. A large literature with many approaches exist on this subject [5,2,1,8,27,18].

In the following, we consider a filtering we proposed in [10]. The main reason is that this filtering process is defined on the power map of the digital medial axis and is well suited to our method. More precisely, the filtering first computes the area of each power cell. Such information is used to evaluate the relevance of a ball since a power cell with small area means that either the ball is small, or the ball is locally surrounded by larger ones. In the following we can just filter the input medial axis using a threshold γ on the power cell area.

Beside its simplicity with respect to some other metrics on local scale relevance of medial balls, such approach leads to a very efficient pre-processing. In fact, this pre-processing is just used to remove some spurious balls in the medial axis induced by small noise on the object surface. The overall segmentation is driven by

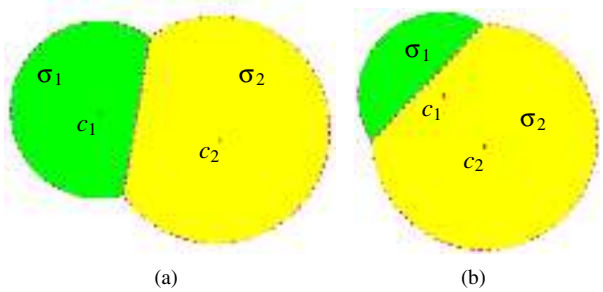

Fig. 3. The definition of digital critical points: c_1, c_2 are the center points of balls and σ_1, σ_2 are their respective power cells. In (a), $c_1 \in \sigma_1$ and $c_2 \in \sigma_2$, c_1 and c_2 are both critical points. In (b), $c_2 \in \sigma_2$, c_2 is a critical point; however $c_1 \in \sigma_2$ too, so c_1 is a regular point.

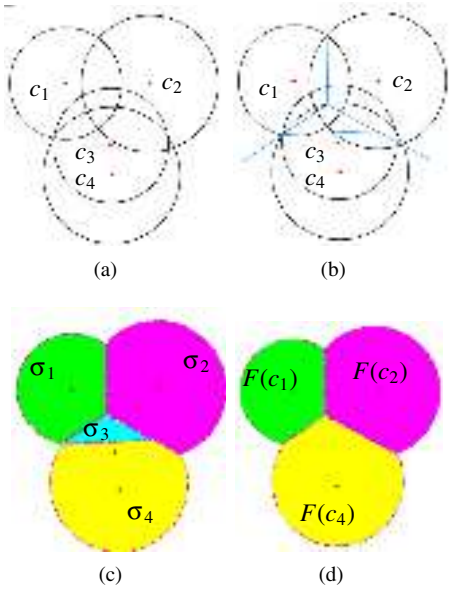

Fig. 4. Digital stable manifold construction: (a) input set of medial balls with centers c_1, c_2, c_3 and c_4, (b) and (c) depict the corresponding power diagram and their associated cells σ_1, σ_2, σ_3 and σ_4. $c_3 \notin \sigma_3$, being regular, we have $l(c_1) = 1$, $l(c_2) = 2$, $l(c_3) = 4$, and $l(c_4) = 4$. (d) illustrates the associated stable manifolds.

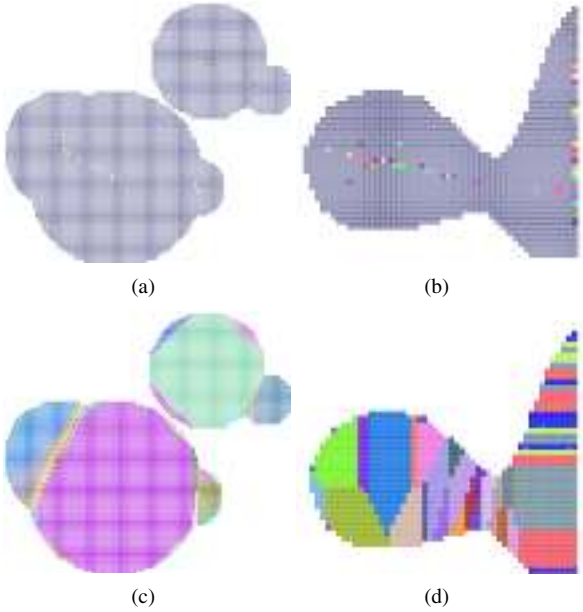

Fig. 5. Digital Medial Axis and Power Map in dimension 2: (a) and (b) discrete medial axes given by the ball centers, (c) and (d) the corresponding power maps.

both critical balls and the merging process as described below, the impact of the ball filtering technique on the results being actually very limited.

5.2. Merging using geometric angle

When considering complex geometrical shapes, stable manifolds usually lead to an over-decomposition of the object (see Fig. 7(a)). We describe here a simple geometric parameter to decide whether two adjacent stable manifolds should be merged.

Let us consider two critical points c_i, c_j (with radii r_i and r_j) with adjacent power cells in Π_X (we use 6 neighborhood in applying to 3-D images). We consider the angle α such that

$$cos(\alpha) = \frac{\|c_i - c_j\|^2 - r_i^2 - r_j^2}{2 \cdot r_i \cdot r_j} \quad (7)$$

Fig. 6 illustrates angles α for two given circles in dimension 2. Similarly, in dimension 3, α corresponds to the angle between tangent vectors of each ball at the intersection between two balls. In the following, we use this quantity to design a simple local criterion: given a threshold $\theta \in [-1, 1]$, if $cos(\alpha) < \theta$ for any two adjacent critical balls, we reassign one of the critical point label. For instance, we set $l(c_i) = j$ (choice between c_i or c_j in the reassignment has no influence on the result). Using different values of θ, we can obtain different decomposition results as shown in Fig. 7. In practice, the choice of such a value depends on the requirements of applications. In our context, θ was normally chosen from -0.6 to -0.8, considering the structure of grains in different snow types.

6. Application to 3-D snow images

The proposed algorithm has been implemented using tools available in DGtal library [9] such as linear in time volumetric algorithms (medial axis extraction, power map,..., [10]). As mentioned above, if the input 3-D object is defined in a $[1 \dots n]^3$ image, both digital medial axis extraction and power map constructions can be performed in $O(n^3)$ [10]. The pre-processing (if needed) can be done using a linear scan of the power map. The merging step criterion is evaluated on each pair of critical points with adjacent power cells. A rough upper bound for the computational cost of this step is given by the size of the power map. This upper bound is not tight since the number of critical points is usually much smaller than the size of the input object. For instance, for the MF sample (Fig. 9(a)) with size 270^3, we have 155281 digital medial balls and 3601 critical points. Finally, the operations on the label function l can be implemented using a Disjoint-Set (or Union-Find) data-structure, which allows us to have all these operations in amortized quasi-constant time. Hence, the overall computational cost of the segmentation algorithm is linear in the size of the input volume.

The proposed algorithm (MADF for short) has been experimented on 3-D images and compared to other decomposition approaches such as watershed with distance function and CDGS (Curvature-Driven Grain Segmentation, [36]) and, when available, to ground truth from physical experiments (DCT, [29] see Section 6.2). In all cases, the provided outputs are volumetric decomposed objects whose components are labelled by different colors. The methods have been applied on both synthetic data and snow microtomographic images.

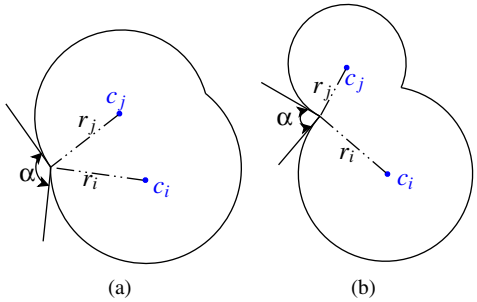

Fig. 6. α Angles for two given configurations of spheres.

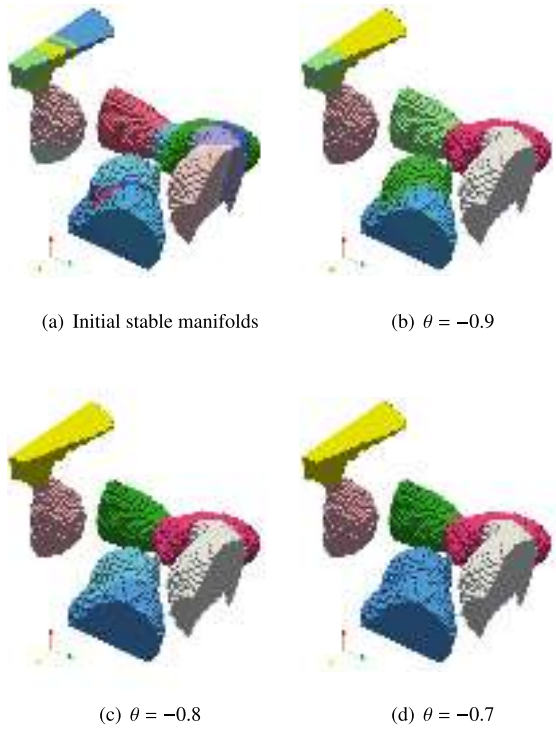

Fig. 7. Decomposition results after the merging step for different θ values: (a) initial digital stable manifolds, (b) – (d): several increasing θ values.

6.1. Experimentation on synthetic data

We first consider series of synthetic 3-D images using randomly generated spheres sets in $[0, 300]^3$. The comparison results are presented in Table 1. For spheres, radii are distributed between R_1 and R_2, N indicates the number of spheres. In order to quantify the difficulty of the decomposition problem, we define the ratio ρ as follows:

$$\rho = \frac{\sum_{i=1}^{N} |B_i| - |X|}{|X|} \quad (8)$$

where $|B_i|$ is the volume of an element in the random spheres set. Hence, high ρ indicate that many geometrical elements overlap and thus recovering each of them is more challenging.

For a better validation, we have created five sphere sets. For each test, we count the number of decomposed grains and quantify the percentage of misclassified voxels when a ground-truth decomposition is known (label "i" in the ground-truth image is associated to the label "j" in the test image if most voxels with label "i" are mapped to label "j" in test image). In these sphere tests, the ground-truth decomposition is given by the power map of input spheres. We use thresholds $\gamma = 0$ and $\theta = -1$ for MADF, because these synthetic images are smooth and the critical point of a sphere is exactly its center. No parameter has been used for watershed and among the large set of parameters for CDGS (13 but 4 main parameters), we have performed a manual analysis to select the best ones for the objects. According to the results in

Table 1
Quantitative results for random spheres (a) and MF sample (b) compared among three decomposition approaches: watershed with distance function, CDGS and MADF.

N	R_1	R_2	ρ	watershed		CDGS		MADF	
				# grains	% misclass.	# grains	% misclass.	# grains	% misclass.
(a)									
100	20	30	0.08408	216	0.728596	100	0.707515	100	0.302259
80	25	35	0.14911	252	1.2033	80	0.765337	80	0.565739
60	30	40	0.19667	251	1.88912	59	1.51798	59	0.8645
40	35	45	0.19068	251	1.8194	39	1.51363	40	0.775526
50	20	80	0.24879	252	4.64338	49	6.11259	50	3.36936

real #grains	watershed		CDGS		MADF	
DCT	# grains	% misclass.	# grains	% misclass.	# grains	% misclass
(b)						
93	31	17.7403	80	3.84519	99	1.83415

Fig. 8 and Table 1(a), watershed method with distance function usually produces an over-decomposition around the interface between two adjacent spheres. It results in a large number of regions in Table 1(a). Such over-segmented regions are small or thin since the percentage of misclassified voxels is still low. CDGS and MADF both present good decomposition results on spheres sets in Fig. 8. Considering the number of decomposed grains and percentage of misclassified voxels, MADF has a more precise decomposition than CDGS.

6.2. Decomposition of snow images

We used 3-D images of real snow samples (see Fig. 9) to evaluate the quality of the shape decomposition provided by the proposed algorithm.

Snow images, such as the RG sample of Fig. 9(b), are obtained by X-ray absorption microtomography using the following technique: the snow samples were first filled with liquid 1-chloronaphthalene around -2 °C and frozen at -25 °C before further machining. Small cores 9 mm in diameter were then extracted with a precision hole-saw, sealed inside sample holders, which were then placed into a specifically designed cryogenic cell for microtomographic acquisition. The obtained gray-level images were contoured using a semi-automatic procedure, leading to binary (air and ice) decomposed 3-D images. Complementary information can be found in previous works of [16,17].

In addition to classical absorption tomography, an image was obtained by Diffraction Contrast Tomography (DCT, [21,29]), a recent experimental technique that combines X-ray diffraction analyses and absorption tomography to provide simultaneously, (1) the 3-D geometry of the ice-air interface, (2) the 3-D mapping of individual grains in polycrystals, and (3) their crystalline orientation. For some particular snow structures such as that of the MF sample presented in Fig. 10(a), each geometric grain exhibits a particular crystalline orientation so that the DCT can actually provide a physically-based shape decomposition of the granular structure.

For the MF sample (Fig. 9(a)), we chose the values $\gamma = 160$ and $\theta = -0.8$ of MADF to decompose the object. For the RG sample (Fig. 9(b)), the values $\gamma = 20$ and $\theta = -0.5$ were adopted. For the watershed method, no parameter has been introduced. For CDGS, among the 13 existing parameters, 4 are crucial to control the quality of decomposition. Interfaces are important to perform numerical simulations on snow grains and MADF produces better and smoother grain-to-grain interface plans than CDGS, as can be seen from Fig. 10(h)–(j). From the decomposition results in Fig. 10 and Table 1(b), we can conclude that a more precise decomposition can be achieved with MADF than with the other two numerical methods.

In Table 2, we have performed a geometrical analysis of the grain-to-grain interfaces. The main idea was to evaluate the quality of the interface in terms of flatness. To do so, we processed all interfaces and we computed several quantities: mean and

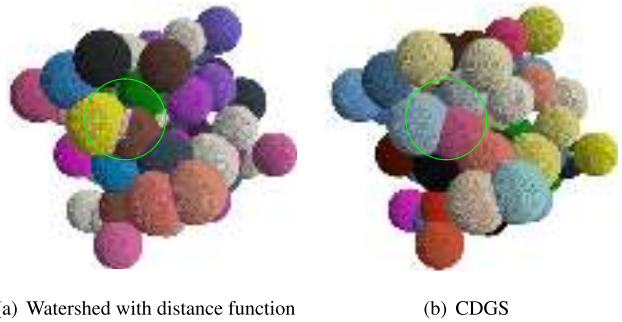

(a) Watershed with distance function (b) CDGS

(c) MADF

Fig. 8. Comparison on random sphere sets by watershed with distance function, CDGS and MADF respectively: (a) an over-decomposition is produced by watershed, (b) and (c) illustrate that both CDGS and MADF (with $\gamma = 0,\ \theta = -1$) work well on sphere sets.

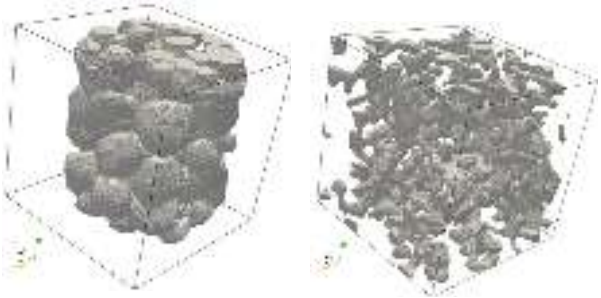

(a) (b)

Fig. 9. 3-D images of snow as obtained by Diffraction Contrast Tomography (a) with size 270^3 (MF sample - all labels of physically detected grains have been set to the same value. See Fig. 10(a) for the original DCT image) and X-ray microtomography (b) with size 256^3 (RG sample).

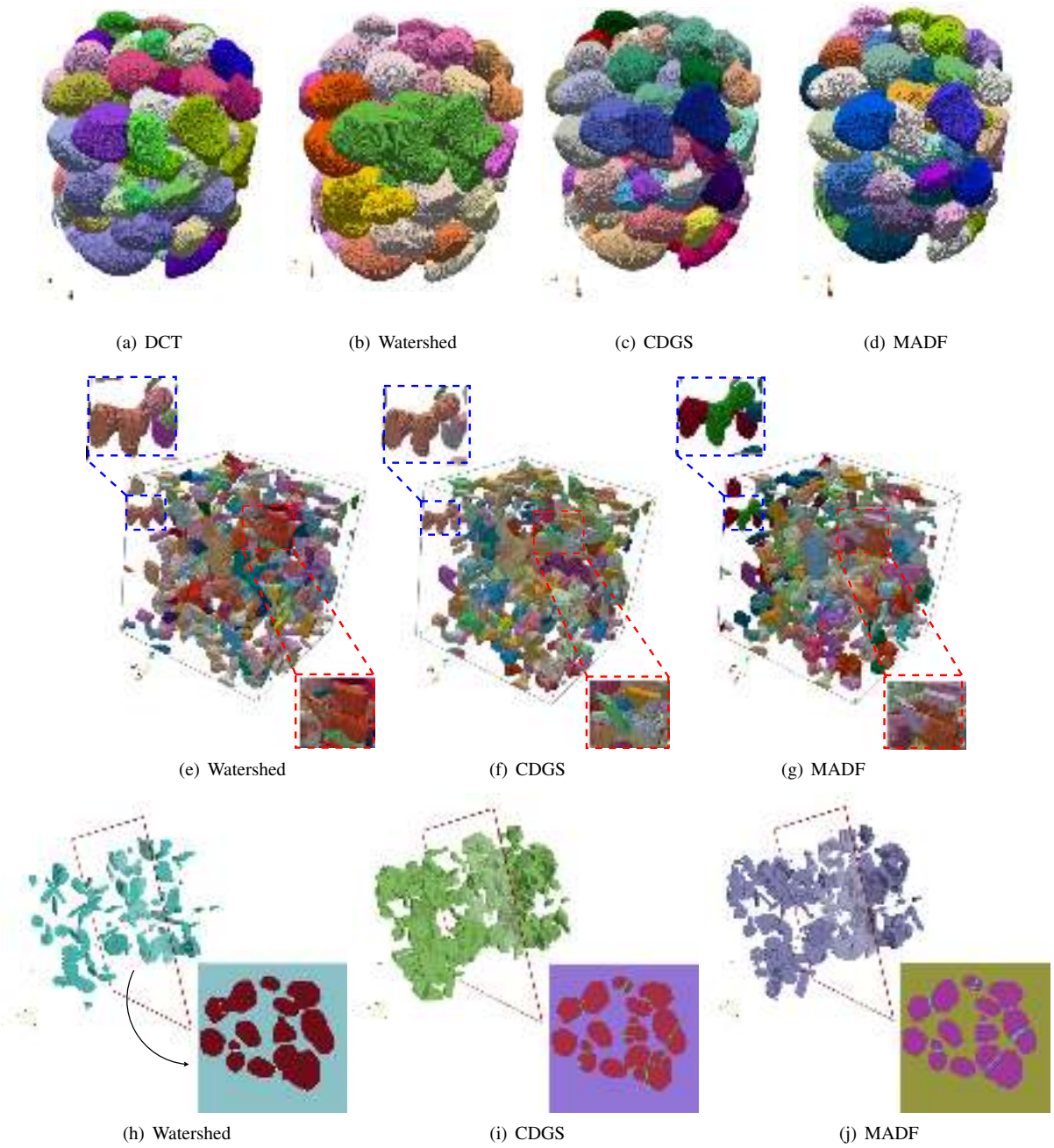

Fig. 10. Comparisons between methods: decomposition of 3-D snow samples MF (a) – (d); decomposition on sample RG (e) – (g); grain-to-grain interfaces of MF comparisons (h) – (j).

Table 2
Comparison of the interface geometry for RG and MF sample among three decomposition approaches: watershed with distance function, CDGS and MADF.

		Watershed		CDGS		MADF	
		average	standard dev.	average	standard dev.	average	standard dev.
MF	Absolute mean curvature	0.055	0.097	0.869	0.221	0.105	0.291
	Absolute Gaussian curvature	0.042	0.313	0.057	0.757	0.027	0.171
	flatness	2.861	6.023	2.094	4.452	0.608	1.815
RG	Absolute mean curvature	0.102	0.152	0.185	1.420	0.186	0.494
	Absolute Gaussian curvature	0.025	0.075	0.974	29.834	0.0845	0.584
	flatness	0.368	0.79	0.541	1.134	0.356	0.616

Gaussian curvatures given by a fitting with high degree polynomial surface of the interface point set [7], and *flatness* information by computing the covariance matrix of the point set and returning the smallest eigenvalues which correspond to the minimal axis

Table 3
Timings for the proposed methods in seconds (Intel (R) Xeon (R) CPU 2.67 GHz/4 Processors/RAM 7.8G).

Shapes	Watershed	CDGS	MADF
MF	416.74	915.44	44 (pre-process time) 10.69 (merging time)
RG	330.732	635.41	40.16 (pre-process time) 7.4 (merging time)

length of the ellipsoid approximating the point set. Beside the watershed approach, which produces flat interfaces but with bad segmentation results, we can observe that the MADF approach provides better quality interfaces than CDGS (lower average values and lower standard deviations).

Finally, Table 3 indicates some timings of the proposed approach.

7. Conclusion

In this paper, we proposed a novel framework for shape decomposition based on digital critical points and the digital flow induced by the medial axis of shape. The core of the approach relies on an adaptation of classical flow and critical points definitions from computational geometry to digital settings. Such an adaptation allows us to construct a fast decomposition algorithm which is computationally efficient and provides high quality object decomposition on both synthetic data and real 3-D images.

Acknowledgments

The authors thank the scientists of the ESRF ID19 beamline and the members of the SNOW-WHITE project (ANR-06-BLAN-0396) for the image acquisition. This work has been mainly funded by the DIGITALSNOW (ANR-11-BS02-009) research grants.

References

[1] N. Amenta, S. Choi, R.K. Kolluri, The power crust, union of balls, and the medial axis transform, Comput. Geom.: Theory Appl. 19 (2001) pp. 127–153. Submitted for publication.
[2] D. Attali, A. Montanvert, Computing and simplifying 2d and 3d continuous skeletons, Comput. Vision Image Underst. 67 (1997) 261–273.
[3] M. de Berg, O. Cheong, M. van Kreveld, M. Overmars, Computational Geometry: Algorithms and Applications, Springer-verlag, 2008.
[4] H. Blum, A transformation for extracting new descriptors of shape, in: W. Wathen-Dunn (Ed.), Models for the Perception of Speech and Visual Form, MIT Press, 1967, pp. 362–380.
[5] G. Borgefors, Distance transformations in digital images, Comput. Vision Graphics Image Process. 34 (1986) 344–371.
[6] J. Brzoska, F. Flin, N. Ogawa, Using Gaussian curvature for the 3D segmentation of snow grains from microtomographic data, Phys. Chem. Ice (2007) 125–132.
[7] F. Cazals, M. Pouget, Estimating differential quantities using polynomial fitting of osculating jets, Comput. Aided Geom. Des. 22 (2005) 121–146.
[8] F. Chazal, A. Lieutier, The lambda-medial axis, Graph. Models 67 (2005) 304–331.
[9] D. Coeurjolly, J.O. Lachaud, et al., Dgtal: Digital geometry tools and algorithms library, 2009.
[10] D. Coeurjolly, A. Montanvert, Optimal separable algorithms to compute the reverse euclidean distance transformation and discrete medial axis in arbitrary dimension, IEEE Trans. Pattern Anal. Mach. Intell. 29 (2007) 437–448.
[11] M. Couprie, D. Coeurjolly, R. Zrour, Discrete bisector function and euclidean skeleton in 2D and 3D, Image Vision Comput. 25 (2007) 1519–1698.
[12] T. Dey, J. Giesen, S. Goswami, Shape segmentation and matching with flow discretization, Lect. Notes Comput. Sci. 2748 (2003) 25–36.
[13] H. Digabel, C. Lantuejoul, Iterative algorithms, CGMM, ENSMP, 1978.
[14] M. Faessel, D. Jeulin, Segmentation of 3D microtomographic images of granular materials with the stochastic watershed, J. Microsc. 239 (2010) 17–31.
[15] C. Fierz, R.L. Armstrong, Y. Durand, P. Etchevers, E. Greene, D.M. McClung, K. Nishimura, P.K. Satyawali, S.A. Sokratov, The international classification for seasonal snow on the ground, IHP-VII Technical documents in hydrology, no. 83, IACS contribution n°1, UNESCO/IHP, Paris, 2009.
[16] F. Flin, J.B. Brzoska, B. Lesaffre, C. Coléou, R.A. Pieritz, Full three-dimensional modelling of curvature-dependent snow metamorphism: first results and comparison with experimental tomographic data, J. Phys. D: Appl. Phys. 36 (2003) A49–A54.
[17] F. Flin, J.B. Brzoska, B. Lesaffre, C. Coléou, R.A. Pieritz, Three-dimensional geometric measurements of snow microstructural evolution under isothermal conditions, Ann. Glaciol. 38 (2004) 39–44.
[18] J. Giesen, B. Miklos, M. Pauly, C. Wormser, The scale axis transform, in: J. Hershberger, E. Fogel (Eds.), Symposium on Computational Geometry, ACM, 2009, pp. 106–115.
[19] W.H. Hesselink, A linear-time algorithm for euclidean feature transform sets, Inf. Process. Lett. 102 (2007) 181–186.
[20] W.H. Hesselink, M. Visser, J.B.T.M. Roerdink, Euclidean skeletons of 3D data sets in linear time by the integer medial axis transform, in: C. Ronse, L. Najman, E. Decencière (Eds.), Mathematical Morphology: 40 Years On (Proceeding of Seventh International Symposium on Mathematical Morphology), Springer, 2005, pp. 259–268.
[21] W. Ludwig, P. Reischig, A. King, M. Herbig, E.M. Lauridsen, G. Johnson, T.J. Marrow, J.Y. Buffière, Three-dimensional grain mapping by X-ray diffraction contrast tomography and the use of Friedel pairs in diffraction data analysis, Rev. Sci. Instrum. 80 (2009) 033905.
[22] L. Najman, H. Talbot, Mathematical Morphology: From Theory to Applications, ISTE Ltd and John Wiley & Sons Inc, 2010.
[23] J.L. Pfaltz, A. Rosenfeld, Computer representation of planar regions by their skeletons, Commun. ACM 10 (1967) 119–122.
[24] I. Ragnemalm, The euclidean distance transform (Ph.D. thesis), Linköping University, Linköping, Sweden, 1993.
[25] E. Remy, E. Thiel, Medial axis for chamfer distances: computing look-up tables and neighbourhoods in 2D or 3D, Pattern Recognit. Lett. 23 (2002) 649–661.
[26] E. Remy, E. Thiel, Exact medial axis with euclidean distance, Image Vision Comput. 23 (2005) 167–175.
[27] D. Reniers, A. Telea, Part-type segmentation of articulated voxel-shapes using the junction rule, Comput. Graphics Forum (Proc. Pacific Graphics08) 27 (2008) 1845–1852.
[28] D. Reniers, A. Telea, Patch-type segmentation of voxel shapes using simplified surface skeletons, Comput. Graphics Forum (Proc. Pacific Graphics08) 27 (2008) 1837–1844.
[29] S. Rolland du Roscoat, A. King, A. Philip, P. Reischig, W. Ludwig, F. Flin, J. Meyssonnier, Analysis of snow microstructure by means of X-ray diffraction contrast tomography, Adv. Eng. Mater. 13 (2011) 128–135.
[30] A. Rosenfeld, J.L. Pfaltz, Sequential operations in digital picture processing, J. ACM 13 (1966) 471–494.
[31] T. Saito, J.I. Toriwaki, Reverse distance transformation and skeletons based upon the euclidean metric for n-dimensionnal digital pictures, IECE Trans. Inf. Syst. E77-D (1994) 1005–1016.
[32] J. Serra, Image Analysis and Mathematical Morphology, Academic Press Inc., 1983.
[33] L. Shapiro, G. Stockman, Computer Vision, Prentice Hall, 2001.
[34] P. Soille, Morphological Image Analysis, Springer-Verlag, Berlin, Heidelberg, New York, 2004.
[35] S. Svensson, G.S. di Baja, Using distance transforms to decompose 3D discrete objects, Image Vision Comput. 20 (2002) 529–540.
[36] X. Wang, L. Gillibert, F. Flin, D. Coeurjolly, Curvature-driven volumetric segmentation of binary shapes: an application to snow microstructure analysis, in: International Conference on Pattern Recognition, IEEE Computer Society, 2012, pp. 742–745.
[37] Y. Zhang, J. Paik, A. Koschan, M.A. Abidi, D. Gorsich, A simple and efficient algorithm for part decomposition of 3D triangulated models based on curvature analysis, in: Proceedings of the International Conference on Image Processing, III, 2002, pp. 273–276.